Numerical simulation of three-component multiphase flows at high density and viscosity ratios using lattice Boltzmann methods

Reza Haghani Hassan Abadi,[1] Abbas Fakhari,[2] and Mohammad Hassan Rahimian[1]
[1]*School of Mechanical Engineering, College of Engineering, University of Tehran, Tehran, Iran*
[2]*Department of Chemical and Biomolecular Engineering, University of Pennsylvania, Pennsylvania 19104, USA*

(Received 23 August 2017; published 22 March 2018)

In this paper, we propose a multiphase lattice Boltzmann model for numerical simulation of ternary flows at high density and viscosity ratios free from spurious velocities. The proposed scheme, which is based on the phase-field modeling, employs the Cahn-Hilliard theory to track the interfaces among three different fluid components. Several benchmarks, such as the spreading of a liquid lens, binary droplets, and head-on collision of two droplets in binary- and ternary-fluid systems, are conducted to assess the reliability and accuracy of the model. The proposed model can successfully simulate both partial and total spreadings while reducing the parasitic currents to the machine precision.

DOI: 10.1103/PhysRevE.97.033312

I. INTRODUCTION

Three-component fluid flows are ubiquitous in many natural phenomena and industrial applications, such as in petroleum engineering, in purifying the water via flotation, and in microfluidic devices, just to name a few. Although experimental studies can reveal the main aspects of a multiphase flow dynamics, it is impractical to investigate all the involved parameters and consider their individual effects. This drawback can be overcome using numerical simulation, which has become an attractive approach in dealing with different physical phenomena, including fluid flow. At the macroscopic level, several multiphase flow solvers based on the Navier-Stokes equations have been introduced, such as level-set [1], volume of fluid [2], and front-tracking schemes [3].

As a mesoscopic approach, the lattice Boltzmann method (LBM) has become an established framework for numerical simulation of fluid dynamics [4,5]. The LBM can readily tackle multiphase flows by incorporating interfacial and intermolecular forces into its kinetic-based equations. Other advantages of the LBM are its ease of implementation, especially on parallel machines [6,7], and its ease of handling complex geometries [8]. In past decades, several two-phase lattice Boltzmann (LB) models have been proposed that can be categorized as: color gradient [9], pseudopotential [10], free-energy [11], and phase-field [12] models. Based on these original two-phase models, some improved variants have also been proposed, e.g., entropic [13] and cascaded [14] LB models, just to name a few. An extensive review of the previously proposed two-phase LB models can be found in Refs. [15,16].

Although all of the above-mentioned LB models can deal with binary, or two-component fluids, little effort has been made to formulate an LB model for ternary fluids. Leclaire *et al.* [17] presented an N-component multiphase LB model based on the color-gradient method [18]. They simulated several stationary problems (at low Reynolds numbers) with density ratios up to 1000. The main shortcoming of their model is that it would be limited to density-matched fluids when dealing with dynamic problems with noticeable topological changes. Bao and Schaefer [19] developed a multicomponent multiphase model based on the pseudopotential model. They simulated stationary problems with density ratios of 1000 and performed dynamic tests with density ratios of 300. They showed that the parasitic currents in their model depend on the density ratio and that their model is able to reduce the parasitic currents down to 0.032 l.u. (l.u. := lattice units) at density ratios of 1000. Based on the free-energy approach, Semprebon *et al.* [20] proposed a LBM for ternary fluids with independently tunable surface tension coefficients. Their model was also limited to density-match fluids for both static and dynamic cases. Shi *et al.* [21] proposed a flux-solver LBM based on the three-component Cahn-Hilliard equation. Because of numerical instability, their model is limited to low density ratios up to 2. Liang *et al.* [22] proposed another ternary LBM based on phase-field modeling. They showed that the maximum density in their model is dependent on the velocity field and that their model can handle static and dynamic problems with density ratios up to 100 and 20, respectively.

In addition to the above-mentioned LB models for three-component fluids, there are other LB schemes that can model amphiphilic mixture fluids, such as oil-water-amphiphile. The first amphiphilic LB model was proposed by Lamura *et al.* [23] based on an appropriate free-energy functional. This LB model is suitable for ternary systems in which an amphiphilic phase (surfactant) exists at the interface of the other two ordinary phases with no orientational degree of freedom. Based on their binary-fluid model [10], Chen *et al.* [24,25] proposed another LB model for amphiphilic mixtures by considering the dipole direction of the amphiphile and its corresponding interaction with other phases.

All the existing LB models for ternary fluids have two major limitations: (a) They are mostly limited to relatively low density ratios, and (b) they suffer from large parasitic currents. Recently, Lee and Liu [26] proposed a LBM for simulation of two-phase flows at high density ratios. This model has been shown to be free from parasitic currents [27] and a reliable scheme in dealing with multiphase flows at relatively high Reynolds numbers [28]. It has also successfully extended and applied to a variety of systems, such as phase change [29], evaporation [30], pool boiling [31], film boiling [32], and combustion [33,34].

In this paper, we extend the aforementioned model [26] from binary fluids to ternary fluids and propose a different LB model for three-component multiphase flows at high density and viscosity ratios without parasitic currents. The fluid properties, such as density, viscosity, and surface tension, of each component can be defined and tuned independently. Additionally, we are able to simulate both total and partial spreadings at high density and viscosity ratios, the phenomena that escape the capabilities of the existing LB models.

The outline of the paper is as follows: in Sec. II, we present the Cahn-Hilliard-based lattice Boltzmann model for ternary fluids at high density ratios. We introduce three different distribution functions, two of which are used to track the interface among three different fluid components, and one of which is used to recover the hydrodynamic properties. In Sec. III, we validate and assess the efficacy of the proposed model by examining various classical benchmarks. Finally, we conclude the paper in Sec. IV.

II. MATHEMATICAL MODELING

A. Cahn-Hilliard theory for ternary fluids

In order to capture the evolution of the interface between different components, the Cahn-Hilliard approach [35] is used in this paper. The evolution of volume fractions for each fluid component is driven by the minimization of a free energy. The three-component free energy for a fluid in a domain Ω is defined by [36,37]

$$\mathcal{F} = \int_{\Omega}\left[\frac{12}{\xi}E + \frac{3}{8}\xi\gamma_1|\nabla C_1|^2 + \frac{3}{8}\xi\gamma_2|\nabla C_2|^2 + \frac{3}{8}\xi\gamma_3|\nabla C_3|^2\right]d\Omega, \tag{1}$$

where E is the bulk free energy, C_i is the order parameter (or the volume fraction) of component i, ξ is the interface thickness which is assumed to be the same among all components, and γ_i is the capillary coefficient for component i and is related to surface tension coefficients according to $\gamma_i = \sigma_{ij} + \sigma_{ik} - \sigma_{jk}$ $(i,j,k = 1\text{–}3)$ in which σ_{ij} denotes the surface tension between components i and j. The following bulk free energy for three-component fluids has been proposed [36,37]:

$$E = \sigma_{12}C_1^2C_2^2 + \sigma_{13}C_1^2C_3^2 + \sigma_{23}C_2^2C_3^2 + C_1C_2C_3(\gamma_1+\gamma_2+\gamma_3) + \Lambda C_1^2C_2^2C_3^2, \tag{2}$$

where Λ is a constant that is nonzero for total spreading. In the context of ternary systems, a so-called spreading parameter for component i defined as $S_i = -\gamma_i$ classifies the system to behave as total spreading (when S_i is positive for at least one component) or partial spreading (when S_i is negative for all components) [36]. For a mixture of three components, the following relation holds among the order parameters:

$$C_1 + C_2 + C_3 = 1, \tag{3}$$

which means that only two of the three order parameters, say C_1 and C_2, are needed to be known, and the third one can be obtained via $C_3 = 1 - C_1 - C_2$.

Theoretically, the volume fraction must be bounded between 0 and 1. This, however, can be easily violated numerically due to the dispersion errors in discretization, resulting in undershooting and overshooting of the order parameter, which is the main reason for numerical instability at high density ratios. To overcome this, enforcing the order parameter between zero and one or using a cutoff value for the local density has been used by some researchers [38–40]. These approaches, however, might cause some discontinuity in the flow field and violate mass conservation. In order to overcome these unwanted features, we propose to add the following term to the right-hand side of Eq. (2):

$$E_0 = \Psi\{C_1^2\text{step}[-\min(0,C_1)] + C_2^2\text{step}[-\min(0,C_2)] + C_3^2\text{step}[-\min(0,C_3)]\}, \tag{4}$$

where Ψ is an arbitrary constant and step is the step function. Equation (4) is used to increase the slope of the bulk free energy outside the Gibbs triangle (where the order parameters might be negative) and prevent its minimum values to become progressively negative in the simulations. A similar idea was used by Lee and Liu [26] to prevent the order parameter from becoming negative when considering solid-fluid interactions. It is worth noting that this term is more effective when dealing with fluid-solid interactions. Although we will show its positive effects on different parameters in the ternary-fluid system, in practice, we only need to implement this term when considering contact line dynamics on solid boundaries. The Gibbs triangle of the bulk free energy of a ternary system [Eq. (2)] plus the additional term in Eq. (4) is shown in Fig. 1 for two different values of Ψ in partial spreading, where $\sigma_{12} = \sigma_{13} = \sigma_{23} = 10^{-4}$ l.u. As can be seen, the free energy possesses a local maximum at each edge of the triangle and a global maximum inside the triangle which means that the bulk free energy has its minimizing states at the corners of the triangle, i.e., $(C_1,C_2,C_3) = (1,0,0)$, $(0,1,0)$, $(0,0,1)$. As can be seen in Fig. 1, the nonzero value of Ψ does not have any effect on the bulk free energy inside the triangle; it only modifies the values of the bulk free energy when the order parameters are negative.

The behavior of a three-component system is governed by the following transport equation:

$$\frac{\partial C_i}{\partial t} + \nabla\cdot(\boldsymbol{u}C_i) = -\nabla\cdot\boldsymbol{J}_i, \quad i = 1-3, \tag{5}$$

where t is the time, $\boldsymbol{u}$ is the macroscopic velocity, and $\boldsymbol{J}_i$ is the volumetric flow rate of component i due to diffusion. Cahn and Hilliard [29] assumed that $\boldsymbol{J}_i$ is proportional to the gradient of the chemical potential, say $\boldsymbol{J}_i = -M_i\nabla\mu_i$ in which $M_i = \frac{M_0}{\gamma_i}$ is the mobility with M_0 being an auxiliary parameter [36,37], and μ_i is the chemical potential of component i that is defined

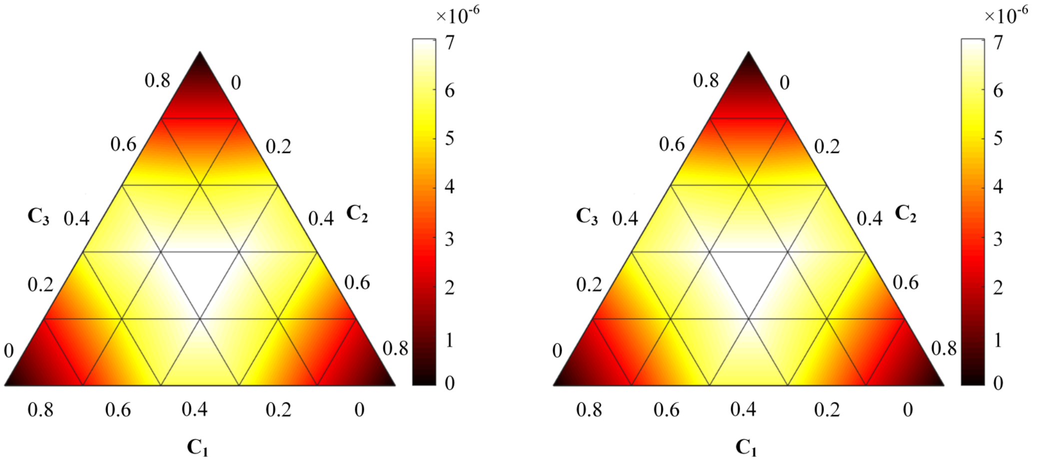

(a) (b)

FIG. 1. Bulk free energy with $\Lambda = 0$ inside the Gibbs triangle, (a) $\Psi = 0$ and (b) $\Psi = 10^{-4}$.

by [36,37]

$$\mu_i = \frac{4\gamma_T}{\xi}\sum_{j\neq i}\left[\frac{1}{\gamma_j}\left(\frac{\partial E}{\partial C_i} - \frac{\partial E}{\partial C_j}\right)\right] - \frac{3}{4}\xi\gamma_i\,\nabla^2 C_i,$$
$$i = 1\text{–}3, \qquad (6)$$

where $\frac{3}{\gamma_T} = (\frac{1}{\gamma_1} + \frac{1}{\gamma_2} + \frac{1}{\gamma_3})$. Therefore, the convective Cahn-Hilliard equation for three-component fluids becomes [36,37]

$$\frac{\partial C_i}{\partial t} + \nabla\cdot(\boldsymbol{u}C_i) = \nabla\cdot(M_i\nabla\mu_i), \quad i = 1\text{–}3. \qquad (7)$$

Note that, in the Cahn-Hilliard equation for ternary fluids (similar to that for binary fluids), there are M_i, γ_i, and ξ on the right-hand side of the governing equation (the diffusion term). Hence, a combination of these parameters can be used as the diffusion coefficient, i.e., $6M_i\gamma_i/\xi$. In this paper the values of the mobility M_i are given in terms of $6M_i\gamma_i/\xi$.

B. Lattice Boltzmann equation for multicomponent fluids

The lattice Boltzmann equation for multiphase fluids with the Bhatnagar-Gross-Krook (BKG) collision operator can be written as [41]

$$\frac{Df_\alpha}{Dt} = \frac{\partial f_\alpha}{\partial t} + \boldsymbol{e}_\alpha\cdot\nabla f_\alpha$$
$$= -\frac{1}{\lambda}\left(f_\alpha - f_\alpha^{\text{eq}}\right) + \frac{(\boldsymbol{e}_\alpha - \boldsymbol{u})\cdot\boldsymbol{F}}{\rho c_s^2}f_\alpha^{\text{eq}}, \qquad (8)$$

where f_α and f_α^{eq} are the distribution function and its equilibrium, respectively, $\boldsymbol{e}_\alpha$ is the mesoscopic velocity set, λ is the relaxation time, ρ is the density, and $c_s = c/\sqrt{3}$ is the lattice speed of sound in which $c = \delta x/\delta t$ is the lattice speed and δx and δt are the grid spacing and time step, respectively. The external force in Eq. (8) is defined by $\boldsymbol{F} = \nabla\rho c_s^2 - \nabla p + \boldsymbol{F}_s$ in which p stands for pressure and the interfacial tension $\boldsymbol{F}_s$ among different components is taken into account through a volumetric force that is zero in the bulk and nonzero within the interface,

$$\boldsymbol{F}_s = \sum_{i=1}^{3}\mu_i\nabla C_i. \qquad (9)$$

For the D2Q9 lattice structure, the mesoscopic velocity set and the equilibrium distribution function are [4] as follows:

$$\boldsymbol{e}_\alpha = \begin{cases} c(0,0), & \alpha = 0,\\ c(\cos\theta_\alpha,\sin\theta_\alpha), & \alpha = 1\text{–}4,\\ \sqrt{2}c(\cos\theta_\alpha,\sin\theta_\alpha), & \alpha = 5\text{–}8, \end{cases} \qquad (10)$$

$$f_\alpha^{\text{eq}}(\rho,\boldsymbol{u}) = \rho w_\alpha\left[1 + \frac{(\boldsymbol{e}_\alpha\cdot\boldsymbol{u})}{c_s^2} + \frac{(\boldsymbol{e}_\alpha\cdot\boldsymbol{u})^2}{2c_s^4} - \frac{(\boldsymbol{u}\cdot\boldsymbol{u})}{2c_s^2}\right], \qquad (11)$$

where w_α is the weighting coefficient set given by $w_0 = \frac{4}{9}$, $w_{1-4} = \frac{1}{9}$, and $w_{5-8} = \frac{1}{36}$.

In order to track the interfaces among the three components, we introduce two new distribution functions as follows:

$$h_\alpha^i = \frac{C_i}{\rho}f_\alpha, \quad i = 1,2, \qquad (12)$$

where the superscript i represents components 1 and 2 and the third component is obtained from Eq. (3). Taking the material derivative of Eq. (12) and applying the trapezoidal integration along characteristics, one can obtain

$$\bar{h}_\alpha^i(\boldsymbol{x} + \boldsymbol{e}_\alpha\delta t, t + \delta t) - \bar{h}_\alpha^i(\boldsymbol{x},t)$$
$$= -\frac{1}{\tau + 0.5}\left(\bar{h}_\alpha^i - \bar{h}_\alpha^{i,\text{eq}}\right)\Big|_{(\boldsymbol{x},t)} + \delta t(\boldsymbol{e}_\alpha - \boldsymbol{u})$$
$$\cdot\left[\nabla^M C_i - \frac{C_i}{\rho c_s^2}\left(\nabla^M p - \sum_{i=1}^{3}\mu_i\nabla^M C_i\right)\right]\Gamma_\alpha\Big|_{(\boldsymbol{x},t)}$$
$$+ \left(\frac{\delta t}{2}M_i\nabla^2\mu_i\right)\Gamma_\alpha\Big|_{(\boldsymbol{x},t)} + \left(\frac{\delta t}{2}M_i\nabla^2\mu_i\right)\Gamma_\alpha\Big|_{(\boldsymbol{x}+\boldsymbol{e}_\alpha\delta t,t)}, \qquad (13)$$

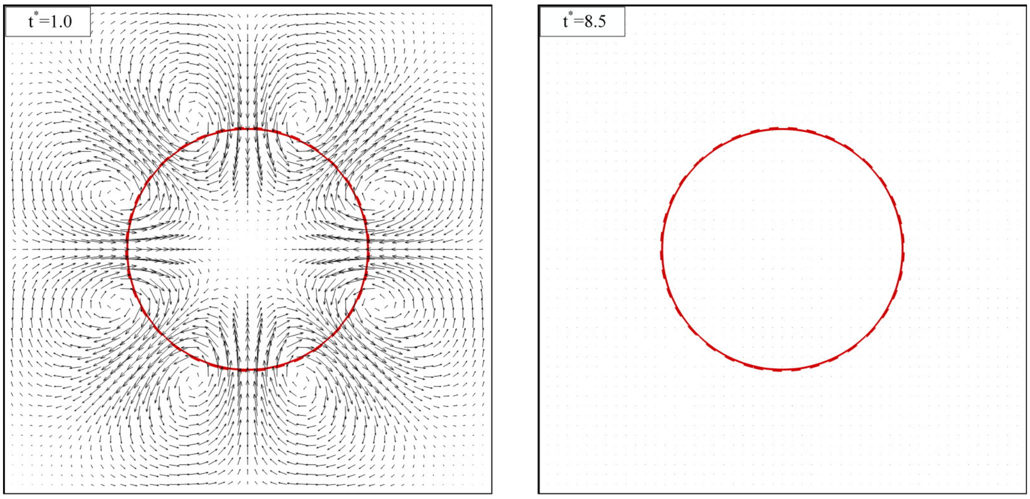

(a) (b)

FIG. 2. Parasitic currents in a binary-fluid setup magnified by (a) 10^8 and (b) 10^{14}. The dashed lines indicate the initial interface location. The red lines indicate $C_1 = 0.5$.

where $\Gamma_\alpha(\boldsymbol{u}) = f_\alpha^{\text{eq}}(\rho,\boldsymbol{u})/\rho$. In the above equation, the modified distribution function $\bar{h}_\alpha^i$ and its equilibrium $\bar{h}_\alpha^{i,\text{eq}}$ are defined as

$$\bar{h}_\alpha^i = h_\alpha^i + \frac{1}{2\tau}\left(h_\alpha^i - h_\alpha^{i,\text{eq}}\right) - \frac{\delta t}{2}(\boldsymbol{e}_\alpha - \boldsymbol{u}) \cdot\left[\nabla^C C_i - \frac{C_i}{\rho c_s^2}\left(\nabla^C p - \sum_{i=1}^{3}\mu_i \nabla^C C_i\right)\right]\Gamma_\alpha, \tag{14}$$

$$\bar{h}_\alpha^{i,\text{eq}} = h_\alpha^{i,\text{eq}} - \frac{\delta t}{2}(\boldsymbol{e}_\alpha - \boldsymbol{u}) \cdot\left[\nabla^C C_i - \frac{C_i}{\rho c_s^2}\left(\nabla^C p - \sum_{i=1}^{3}\mu_i \nabla^C C_i\right)\right]\Gamma_\alpha, \tag{15}$$

in which $h_\alpha^{i,\text{eq}} = C_i f_\alpha^{\text{eq}}/\rho$. In order to enforce incompressibility and avoid numerical instability for obtaining the pressure and velocity fields, we use the following change in variable as suggested by He *et al.* [12]:

$$g_\alpha = f_\alpha c_s^2 + \left(p - \rho c_s^2\right) w_\alpha. \tag{16}$$

Taking the material derivative of g_α and using Eq. (8) yields

$$\frac{Dg_\alpha}{Dt} = \frac{\partial g_\alpha}{\partial t} + \boldsymbol{e}_\alpha \cdot \nabla g_\alpha = -\frac{1}{\lambda}\left(g_\alpha - g_\alpha^{\text{eq}}\right) + (\boldsymbol{e}_\alpha - \boldsymbol{u}) \cdot\left[\nabla \rho c_s^2(\Gamma_\alpha - w_\alpha) + \left(\sum_{i=1}^{3}\mu_i \nabla C_i\right)\Gamma_\alpha\right], \tag{17}$$

in which $g_\alpha^{\text{eq}} = w_\alpha(p + \rho c_s^2[\frac{\boldsymbol{e}_\alpha \cdot \boldsymbol{u}}{c_s^2} + \frac{(\boldsymbol{e}_\alpha \cdot \boldsymbol{u})^2}{2c_s^4} - \frac{(\boldsymbol{u}\cdot\boldsymbol{u})}{2c_s^2}])$ is the new equilibrium distribution function. As can be seen in Eq. (17), the gradient of the density is now multiplied by $(\Gamma_\alpha - w_\alpha)$, which is an order of magnitude smaller than $(\boldsymbol{e}_\alpha - \boldsymbol{u})$ in Eq. (8). This improves the numerical stability at higher density ratios. Integrating Eq. (17) using the trapezoidal rule gives us the following LB equation for recovering the hydrodynamics:

$$\bar{g}_\alpha(\boldsymbol{x} + \boldsymbol{e}_\alpha \delta t, t + \delta t) - \bar{g}_\alpha(\boldsymbol{x},t) = -\frac{1}{\tau + 0.5}\left(\bar{g}_\alpha - \bar{g}_\alpha^{\text{eq}}\right)\Big|_{(\boldsymbol{x},t)} + \delta t(\boldsymbol{e}_\alpha - \boldsymbol{u}) \cdot\left[\nabla^M \rho c_s^2(\Gamma_\alpha - w_\alpha) + \left(\sum_{i=1}^{3}\mu_i \nabla^M C_i\right)\Gamma_\alpha\right]\Bigg|_{(\boldsymbol{x},t)}, \tag{18}$$

where $\tau = \lambda/\delta t$ is the nondimensional relaxation time which is related to the kinematic viscosity by $\nu = \tau c_s^2 \delta t$, and $\bar{g}_\alpha$ and $\bar{g}_\alpha^{\text{eq}}$ are the modified hydrodynamic distribution function and its equilibrium, respectively, which are defined by

$$\bar{g}_\alpha = g_\alpha + \frac{1}{2\tau}\left(g_\alpha - g_\alpha^{\text{eq}}\right) - \frac{\delta t}{2}(\boldsymbol{e}_\alpha - \boldsymbol{u}) \cdot\left[\nabla^C \rho c_s^2(\Gamma_\alpha - w_\alpha) + \left(\sum_{i=1}^{3}\mu_i \nabla^C C_i\right)\Gamma_\alpha\right], \tag{19}$$

$$\bar{g}_\alpha^{\text{eq}} = g_\alpha^{\text{eq}} - \frac{\delta t}{2}(\boldsymbol{e}_\alpha - \boldsymbol{u}) \cdot\left[\nabla^C \rho c_s^2(\Gamma_\alpha - w_\alpha) + \left(\sum_{i=1}^{3}\mu_i \nabla^C C_i\right)\Gamma_\alpha\right]. \tag{20}$$

In the above equations, the superscripts C and M on the gradients stand for the second-order central and mixed (arithmetic average of central and biased) finite differences, respectively [26]. Specifically, for a scalar variable ϕ we use

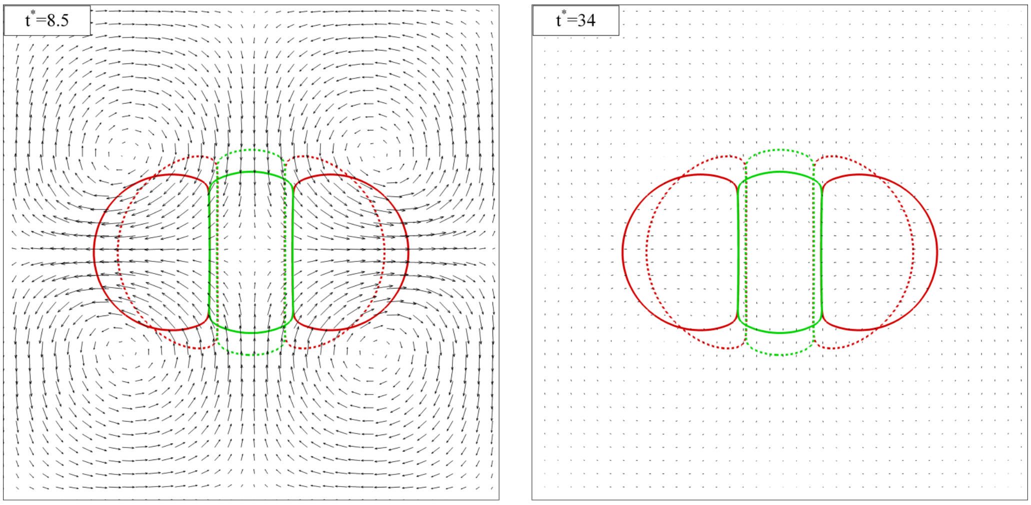

(a) (b)

FIG. 3. Parasitic currents in a ternary-fluid system magnified by (a) 10^8 and (b) 10^{14}. The dashed lines indicate the initial interface location. The red and green lines indicate $C_1 = 0.5$ and $C_2 = 0.5$, respectively.

the following relations:

$$\begin{aligned}
\boldsymbol{e}_\alpha \cdot \nabla^C \phi|_{(\boldsymbol{x},t)} &= \frac{1}{2}[\phi(\boldsymbol{x}+\boldsymbol{e}_\alpha\delta t,t) - \phi(\boldsymbol{x}-\boldsymbol{e}_\alpha\delta t,t)],\\
\boldsymbol{e}_\alpha \cdot \nabla^M \phi|_{(\boldsymbol{x},t)} &= \frac{1}{4}[-\phi(\boldsymbol{x}+2\boldsymbol{e}_\alpha\delta t,t) + 5\phi(\boldsymbol{x}+\boldsymbol{e}_\alpha\delta t,t)\\
&\quad - 3\phi(\boldsymbol{x},t) - \phi(\boldsymbol{x}-\boldsymbol{e}_\alpha\delta t,t)],\\
\nabla^C \phi|_{(\boldsymbol{x},t)} &= \frac{1}{c_s^2\delta t}\sum_{\alpha\neq 0} w_\alpha \boldsymbol{e}_\alpha(\delta t\ \ \boldsymbol{e}_\alpha \cdot \nabla^C)\phi|_{(\boldsymbol{x},t)},\\
\nabla^M \phi|_{(\boldsymbol{x},t)} &= \frac{1}{c_s^2\delta t}\sum_{\alpha\neq 0} w_\alpha \boldsymbol{e}_\alpha(\delta t\ \boldsymbol{e}_\alpha \cdot \nabla^M)\phi|_{(\boldsymbol{x},t)},\\
\nabla^2 \phi|_{(\boldsymbol{x},t)} &= \frac{2}{c_s^2\delta t^2}\sum_{\alpha\neq 0} w_\alpha[\phi(\boldsymbol{x}+\boldsymbol{e}_\alpha\delta t,t) - \phi(\boldsymbol{x},t)].
\end{aligned}$$

The order parameters, velocity, and pressure can be calculated by taking the zeroth and first moments of the distribution functions as follows:

$$C_i = \sum_\alpha \bar{h}_\alpha^i, \quad i = 1,2, \tag{21a}$$

$$\boldsymbol{u} = \frac{1}{\rho c_s^2}\sum_\alpha e_\alpha \bar{g}_\alpha + \frac{\delta t}{2\rho}\left(\sum_{i=1}^{3} \mu_i \nabla^C C_i\right), \tag{21b}$$

$$p = \sum_\alpha \bar{g}_\alpha + \frac{\delta t}{2}\,\boldsymbol{u}\cdot\nabla^C \rho c_s^2. \tag{21c}$$

The local density of the fluid is calculated by a linear interpolation $\rho = \sum_{i=1}^{3} C_i \rho_i$ in which ρ_i is the bulk density of component i. The dimensionless relaxation time is also updated by [37]

$$\tau = (\tau_1 - \tau_3)H(C_1 - 0.5) + (\tau_2 - \tau_3)H(C_2 - 0.5) + \tau_3, \tag{22}$$

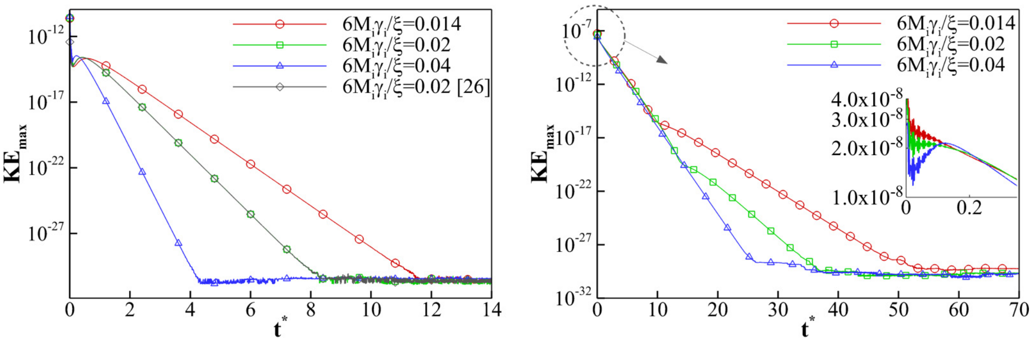

(a) (b)

FIG. 4. Maximum kinetic energy versus dimensionless time for (a) a binary fluid and (b) a ternary fluid.

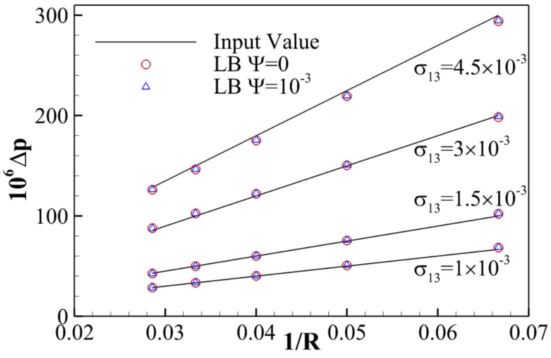

FIG. 5. Verification of the Laplace test.

where H is the Heaviside function. It is possible that the order parameters fluctuate out of their bulk values (0 and 1). These fluctuations tend to increase as the density and viscosity ratios increase. Using Eq. (22) prevents excessive fluctuations in physical parameters.

III. NUMERICAL RESULTS

A. Droplets in a quiescent fluid

To probe the consistency of the present LB model, first a system consisting of a single stationary droplet is considered (C_2 is initially set to zero). All the parameters will be presented either in lattice units or in dimensionless form, unless otherwise stated. A two-dimensional (2D) droplet is placed at the center of a computational domain with 100 × 100 lattice nodes. Periodic boundary conditions are imposed on all the boundaries. The fluid properties are $\rho_1 = 1$, $\rho_3 = 0.1$, $\tau_1 = \tau_3 = 0.5$, and $\sigma_{13} = 10^{-4}$. The interfacial thickness is set to $\xi = 4$ and $6M_i\gamma_i/\xi = 0.02$. Here, the dimensionless time is defined as $t^* = t/(\eta_1 R/\sigma_{13})$, where t is the number of iterations and η_1 is the dynamic viscosity of the heavy fluid. Figure 2 depicts the parasitic currents in the binary-fluid setup. As can be seen, the results are in agreement with those of the two-component model in Ref. [26]. As shown in Fig. 2, the present model is capable of eliminating parasitic currents to the machine precision.

Now we consider a ternary-fluid setup with triple junction points. Three incomplete droplets in contact with each other are generated in a computational domain of size 150 × 150 lattice nodes (see Fig. 3). The properties of the added droplet (the second component) are $\rho_2 = 0.5$, $\tau_2 = 0.5$, and $\sigma_{12} = \sigma_{23} = 10^{-4}$. The boundary conditions and other physical parameters are the same as those in the binary-fluid setup.

Figure 3 depicts the parasitic currents for the three-component fluid. Similar to the two-component fluid, the three-component model is capable of eliminating parasitic currents to the machine precision even when triple junction points exist.

The variation of the maximum kinetic energy ($\mathrm{KE}_{\max}$) of the fluid versus time for the binary-fluid test (in Fig. 2) and ternary-fluid test (in Fig. 3) is shown in Fig. 4 for different values of the mobility. In the absence of one component [Fig. 4(a)], the proposed model is in agreement with its two-component counterpart [26], showing the consistency of the model. It is worth noting that using higher $6M_i\gamma_i/\xi$ leads to a faster dampening of the parasitic currents and a faster convergence toward the equilibrium state.

As a benchmark problem, the Laplace test is also conducted. According to the Laplace law, the pressure difference across the interface of a 2D droplet is related to the surface tension via

$$\Delta p = p_{\mathrm{in}} - p_{\mathrm{out}} = \frac{\sigma}{R}. \tag{23}$$

In order to verify the Laplace law, the radii of one droplet (filled with component 1 and surrounded with component 3) are varied from 15 to 35 in a domain with 200 × 200 lattice sites. Periodic boundary conditions are imposed on all the boundaries, and the following parameters are used: $\rho_1 = 1$, $\rho_3 = 0.001$, $\tau_1 = \tau_3 = 0.5$, and $\Lambda = 0$. The results are shown in Fig. 5 for four different values of surface tension coefficients. As can be seen in Fig. 5, the results are in good agreement with the theoretical solution.

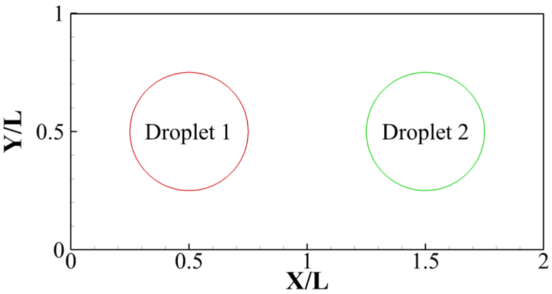

FIG. 6. Two cylindrical droplets in a ternary-fluid system.

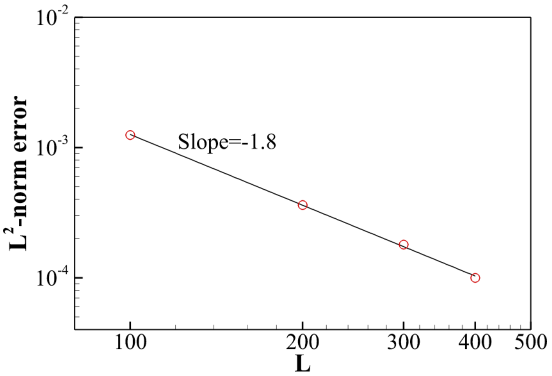

FIG. 7. L^2-norm error versus number of grids in the y direction.

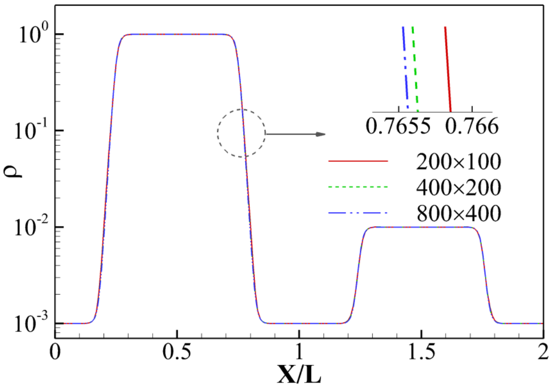

FIG. 8. Density profile versus dimensionless distance for three different grid resolutions.

B. Two stationary droplets

In this subsection, the classical problem of two circular droplets that are placed apart from each other in a quiescent fluid is investigated. The problem setup is shown in Fig. 6. First, convergence analysis and grid independency of the results are examined for different grid resolutions. Two droplets with radii of $R = L/4$ are located $4R$ apart (center to center) in a domain with $2L \times L$ lattice sites, where $L = 100$, 200, and 400. The fluid properties are as follows: $\rho_1 = 1$, $\rho_2 = 0.01$, $\rho_3 = 0.001$, $\sigma_{12} = \sigma_{13} = \sigma_{23} = 10^{-4}$, $\tau_1 = \tau_2 = \tau_3 = 0.5$, $\Lambda = 0$, and $\Psi = 10^{-4}$. The L^2-norm error of the nearest distance l of the two droplets is defined as $E_{L^2} = \sqrt{\frac{(l_{\text{LBM}} - l_0)^2}{l_0^2}}$, where l_0 is the initial distance. Figure 7 shows the L^2-norm error for different grid resolutions. As can be seen, close to second-order convergence is achieved. The grid independency of the results is also shown in Fig. 8.

To investigate the effects of the additional term in the free energy [Eq. (4)], the maximum and minimum values of the order parameters in the computational domain are monitored and plotted in Fig. 9 for $L = 200$. Initially, the numerical values of the order parameters lie between 0 and 1. The maximum values of C_1 and C_2 increase rapidly at early times and then exponentially decrease until they reach their new equilibrium values [Fig. 9(a)]. It should be mentioned that, because we use two distribution functions for tracking two of the interfaces (C_1 and C_2) and the other order parameter (C_3) is obtained from Eq. (3), the evolution of the maximum value of C_3 is different than those of C_1 and C_2. Figure 9(b) shows that the minimum values of C_1 and C_2 become negative at early times and then start to rise until they reach a steady state. As can be seen in Fig. 9, using the additional term [Eq. (4)] in the free energy limits the variation of the order parameter for each component and reduces the magnitude of the fluctuations by about 50%.

To investigate the effects of Ψ in more detail, the profiles of the order parameters along the centerline ($y = 100$) are shown in Fig. 10. It can be seen that at the interface of the two components the other component also exists, which is a numerical artifact. Using a nonzero value for Ψ (symbols) improves this behavior.

C. Spreading of a liquid lens

Spreading of a liquid lens is another benchmark used for validation of the three-component fluids with triple conjunctions. A computational domain with 250 × 150 lattice sites is used with periodic boundary conditions in the x direction and no-slip boundary conditions at the bottom and top. A droplet with a radius of $R = 30$ is located in the center of the interface of the other two components. Five sets of surface tension coefficients, namely, $(\sigma_{12},\sigma_{13},\sigma_{23}) = (10^{-4},10^{-4},10^{-4})$, $(6 \times 10^{-5},6 \times 10^{-5},10^{-4})$, $(8 \times 10^{-5},1.4 \times 10^{-4},10^{-4})$, $(10^{-4},3 \times 10^{-4},10^{-4})$, and $(10^{-4},10^{-4},3 \times 10^{-4})$, are considered in our simulations. The fluid properties are as follows: $\rho_1 = 1$, $\rho_2 = 0.05$, $\rho_3 = 0.001$, $\tau_1 = 0.05$, and $\tau_2 = \tau_3 = 0.5$. Furthermore, the following parameters are used: $\xi = 4$, $6M_i\gamma_i/\xi = 0.02$, $\Lambda = 0.004$, and $\Psi = 10^{-4}$. Using the aforementioned parameters, both partial and total spreading mechanisms will be simulated.

In addition to the Laplace-Young relation (24) between surface tension coefficients and contact angles, the distance between the triple junctions d can be related to contact angles

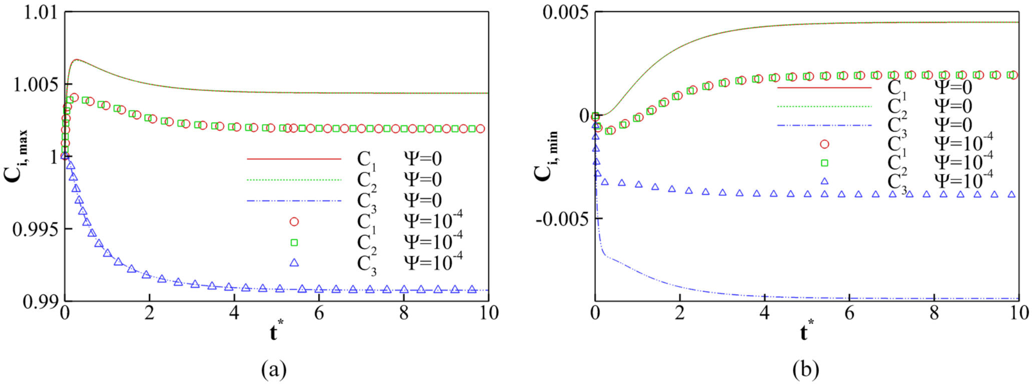

(a) (b)

FIG. 9. Evolution of (a) the maximum values of order parameters ($C_{i,\max}$) and (b) the minimum values of order parameters ($C_{i,\min}$) versus dimensionless time.

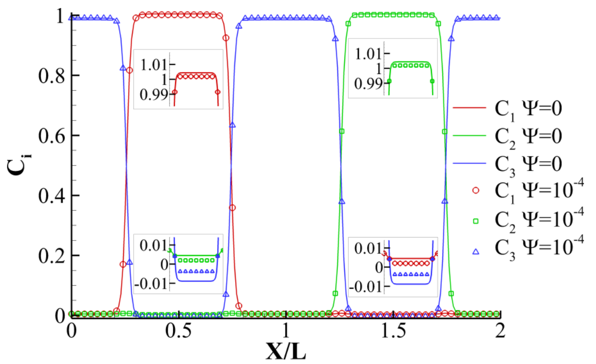

FIG. 10. Profiles of the three order parameters along the center line ($y = 100$) at $t^* = 10$.

according to Young's relation [also see Fig. 11(a)] [42],

$$\frac{\sin(\theta_1)}{\sigma_{23}} = \frac{\sin(\theta_2)}{\sigma_{13}} = \frac{\sin(\theta_3)}{\sigma_{12}}, \tag{24}$$

$$d = \left[\frac{8A\sin^2(\pi-\theta_2)}{2(\pi-\theta_2)-\sin[2(\pi-\theta_2)]} + \frac{8A\sin^2(\pi-\theta_3)}{2(\pi-\theta_3)-\sin[2(\pi-\theta_3)]}\right]^{1/2}, \tag{25}$$

where A is the area of the fluid lens at equilibrium. In 2D, the final shape of the lens (in the case of partial spreading) is a combination of the two circular arcs, and the Laplace law gives us the pressure difference among the three

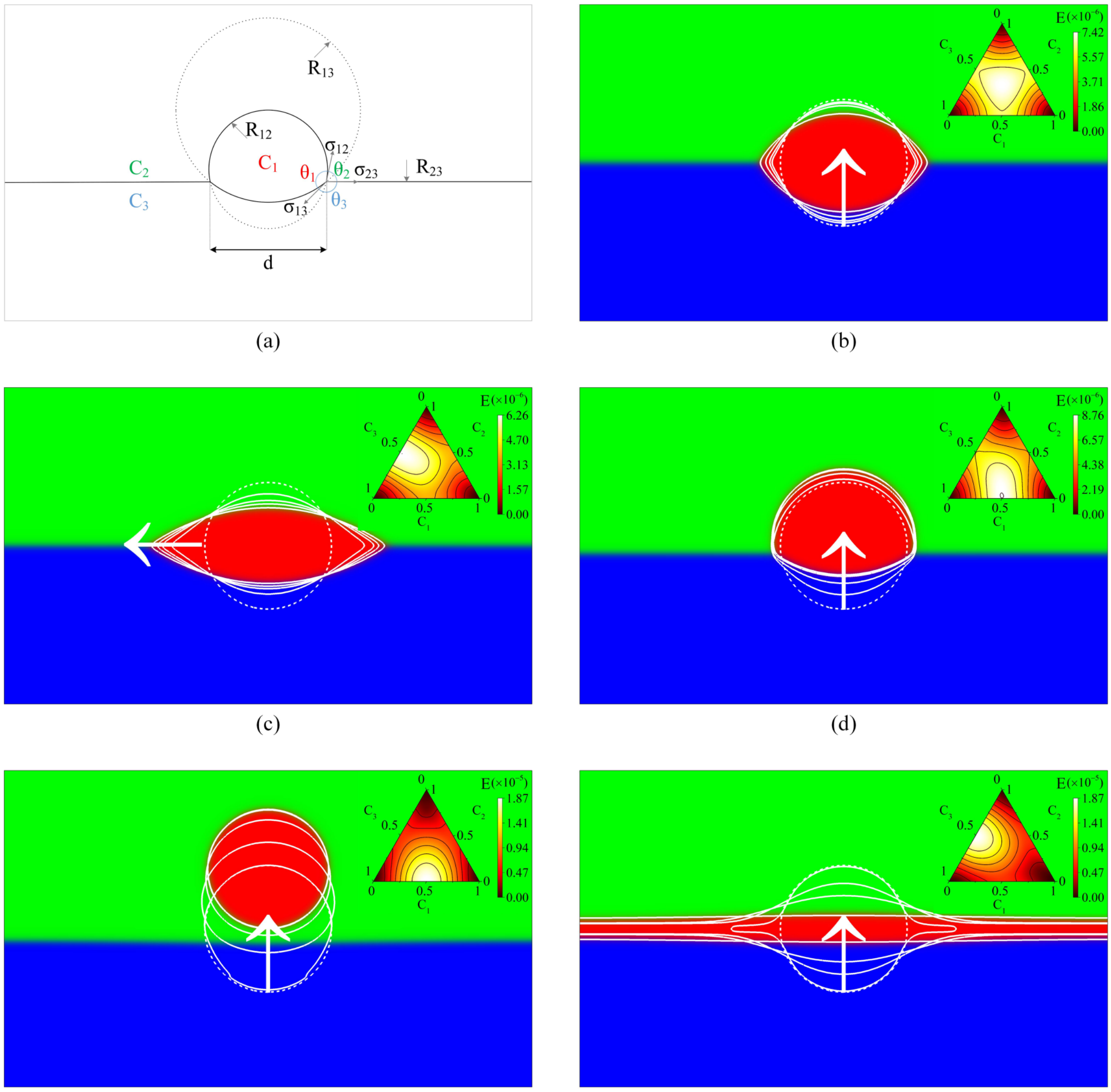

(a) (b)

(c) (d)

(e) (f)

FIG. 11. Time evolution of a circular liquid lens between two layers (a) a schematic of the problem. Surface tension coefficients (σ_{12},σ_{13},σ_{23}) are set to (b) (10^{-4},10^{-4},10^{-4}), (c) (6×10^{-5},6×10^{-5},10^{-4}), (d) (8×10^{-5},1.4×10^{-4},10^{-4}), (e) (10^{-4},3×10^{-4},10^{-4}), and (f) (10^{-4},10^{-4},3×10^{-4}). The dashed line shows the initial position of the liquid lens.

TABLE I. Triple junction distance and pressure difference.

Surface tension coefficients (σ_{12},σ_{13},σ_{23})	Triple junction distance (d) Equation (25)	Numerical results	Relative error (%)	Pressure difference Equation (26)	Numerical results	Relative error (%)
(10^{-4},10^{-4},10^{-4})	83.10	80.62	2.99	2.084×10^{-6}	2.134×10^{-6}	2.40
(6×10^{-5},6×10^{-5},10^{-4})	117.55	113.07	3.81	5.643×10^{-7}	5.922×10^{-6}	4.94
(8×10^{-5},1.4×10^{-4},10^{-4})	67.723	66.046	2.48	2.315×10^{-6}	2.378×10^{-6}	2.72

components,

$$\frac{\sigma_{12}}{R_{12}} = P_1 - P_2 = P_1 - P_3 = \frac{\sigma_{13}}{R_{13}}. \qquad (26)$$

As shown in Table I, satisfactory agreement between the simulation results and the analytical solutions is obtained.

The time evolution of the liquid lens for each set of surface tension is also shown in Fig. 11. Also included in this figure is the Gibbs triangle for comparing the free energy of each set of surface tension. As can be seen in the partial spreading cases [Figs. 11(b)–11(d)], the free energy possesses a global maximum inside the Gibbs triangle which causes the mixed fluid to separate into its components, whereas in the total spreading cases [Figs. 11(e) and 11(f)], the free energy has its global maximum outside the Gibbs triangle such that the separation does not occur without a nonzero value of Λ. In other words, using a nonzero value for Λ makes the free energy have a global maximum inside the triangle.

A comparative study of the effect of three different interpolation schemes, namely, linear ($\tau = \tau_1 C_1 + \tau_2 C_2 + \tau_3 C_3$), harmonic ($1/\tau = C_1/\tau_1 + C_2/\tau_2 + C_3/\tau_3$), and Heaviside [Eq. (22)] on the evolution of the relaxation time across a planar interface is performed in Fig. 12. The order parameter is prescribed in such a way to change smoothly across the interface from -0.01 to $+1.01$ instead of 0 to 1 to account for the numerical overshooting and undershooting of the order parameter in actual simulations (see Sec. II B). As shown in Fig. 12, both linear and Heaviside interpolations of the relaxation time are symmetric around $z = z_0$, whereas there is a noticble shift towards higher values of the relaxation time when the harmonic interpolation is used. Overshooting and undershooding of the order parameters cause the linear and harmonic interpolations to take different values of relaxation time than their specified bulk values (in Fig. 12, each inset shows a magnified view of the relaxation time obtained from using each interpolation). In contrast, the Heaviside interpolation keeps the relaxation times bounded within their specified bulk values. To investigate the effect of different interpolations on interface motion, the spreading of a liquid lens [the case in Fig. 11(e)] with different interpolation schemes was conducted, and the results are shown in Fig. 13. The contour of $C_2 = 0.5$ is plotted for two dimensionless times, namely, $t^* = 2$ (the black lines) and $t^* = 5$ (the red lines). As can be seen, the results obtained using the harmonic interpolation are different from those using linear and Heaviside relations due to the undershooting and overshooting of the relaxation time across the interface. At $t^* = 2$, the liquid lens obtained using the Heaviside (the dashed line) and linear (the dashed-dotted line) relations is not separated from the lower fluid, whereas a separation has happened when the harmonic interpolation (the solid line) is used. Although the separation of the interface has occurred earlier, the eventual outcome is different, and the submerged droplet is in a lower position compared to the situation where the linear or Heaviside relations are used. Therefore, in what follows, we employ the Heaviside interpolation for updating the relaxation time.

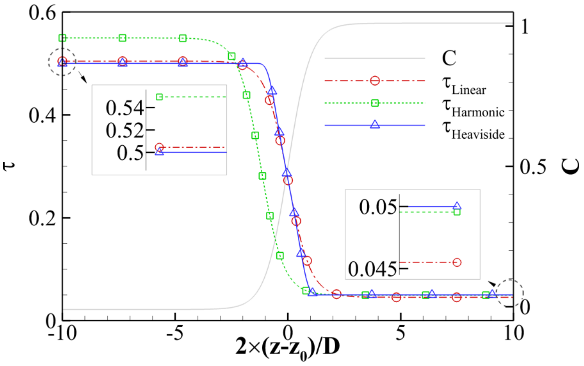

FIG. 12. Profiles of dimensionless relaxation time across the interface ($\tau_1 = 0.05$ and $\tau_2 = \tau_3 = 0.5$).

D. Binary droplet collision in binary and ternary fluids

In this section, we model the collision dynamics between two droplets either with the same physical properties or different physical properties that are surrounded by another fluid component. The collision between different immiscible droplets in a ternary-fluid system [43–50] has different characteristics than that in the binary-fluid system. In addition to new collision outcomes, e.g., single reflexive separation [44] and

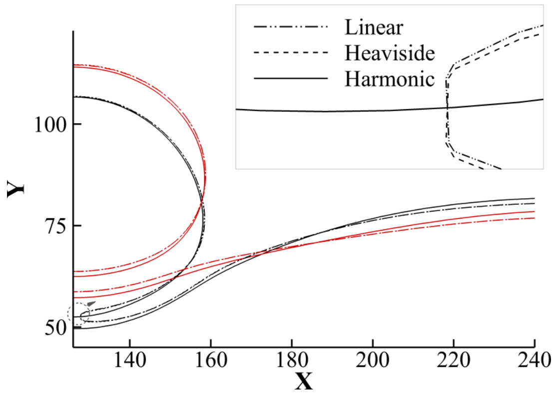

FIG. 13. Contour of $C_2 = 0.5$ for $t^* = 2$ (the black colors) and $t^* = 5$ (the red colors). $\rho_1 = 1$, $\rho_2 = 0.05$, $\rho_3 = 0.001$, (σ_{12},σ_{13},σ_{23}) = (10^{-4},3×10^{-4},10^{-4}), $\tau_1 = 0.05$, $\tau_2 = \tau_3 = 0.5$, and $\Lambda = 0.004$.

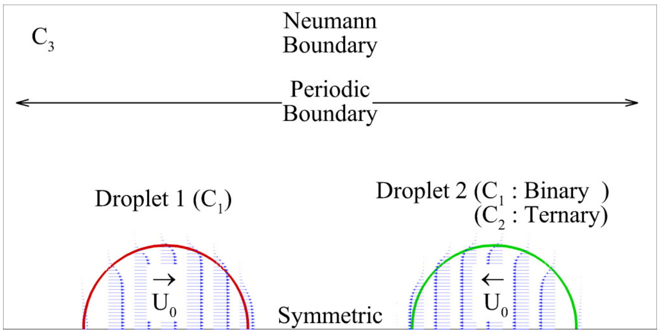

FIG. 14. Schematic of the problem setup for droplet collision.

crossing separation [46], encapsulating one fluid in the shells of the other due to different surface tension coefficients (total spreading) is one of the most interesting features of immiscible droplet collision which is useful in some technical applications, such as drug delivery [46,51]. Our aim here is to demonstrate the ability of the present model in handling immiscible droplet collisions with high density and viscosity contrast for both partial and total spreading scenarios.

A 2D domain with 400 × 250 lattice sites is used for this purpose. The boundary conditions are symmetric at the bottom, Neumann at the top, and periodic in the x direction. Two circular droplets with the same radii of $R = 40$ are placed $4R$ apart from center to center. The surrounding gas component is initially at rest, and after 5000 iterations the droplets are given a uniform velocity towards each other. A schematic of the problem is shown in Fig. 14. In addition to two density ratios $(\rho_1^* = \rho_1/\rho_3,\ \rho_2^* = \rho_2/\rho_3)$ and two viscosity ratios $(\eta_1^* = \eta_1/\eta_3,\ \eta_2^* = \eta_2/\eta_3)$, the dynamic behavior of this head-on collision is described by four dimensionless parameters, namely, the Weber number (We) and the Ohnesorge number (Oh) of each droplet,

$$\mathrm{We}_1 = \frac{2\rho_1 U_{\mathrm{rel}}^2 R}{\sigma_{13}}, \quad \mathrm{We}_2 = \frac{2\rho_2 U_{\mathrm{rel}}^2 R}{\sigma_{23}}, \tag{27}$$

$$\mathrm{Oh}_1 = \frac{16\eta_1}{\sqrt{\rho_1 R \sigma_{13}}}, \quad \mathrm{Oh}_2 = \frac{16\eta_2}{\sqrt{\rho_2 R \sigma_{23}}}, \tag{28}$$

where ρ_1 and η_1 are the density and viscosity, respectively, of the first component (the droplet on the left), ρ_2 and η_2 are the density and viscosity, respectively, of the second component (the droplet on the right), and $U_{\mathrm{rel}} = 2U_0$ is the relative velocity of the droplets. The factor 16 in the definition of the Ohnesorge number is included for consistency with the experimental work of Qian and Law [52] and with the numerical work of Premnath and Abraham [53]. The dimensionless time is defined by $t^* = tU_{\mathrm{rel}}/D$ such that $t^* = 0$ represents the moment when the droplets are set into motion. It is worth noting that the second set of the aforementioned dimensionless groups is solely used for the ternary-fluid system.

We will first validate the proposed ternary LBM by setting the order parameter of one of the components to 0. In other words, we first consider the collision between two droplets of the same fluid that are surrounded by another (different) fluid by setting $C_2 = 0$. Figure 15 illustrates the results obtained using the current LB model and the experimental observations [52] at $\rho_1^* = 666$, $\eta_1^* = 119$, $\mathrm{We}_1 = 32.8$, and $\mathrm{Oh}_1 = 0.615$. A qualitative comparison between the 2D results and the three-dimensional (3D) LB simulations [53] is also provided in Fig. 16 for $\rho_1^* = 4$, $\eta_1^* = 4$, $\mathrm{We}_1 = 20$, and $\mathrm{Oh}_1 = 0.589$. As can be seen in Figs. 15 and 16, satisfactory agreement between the 2D results and the available experimental and numerical data is obtained.

Now, we will consider the head-on collision of two droplets of different fluids in a third component, that is, the binary droplet collision in a ternary-fluid system. Four different sets for surface tension coefficients are chosen as listed in Table II. In order to compare the results between binary and ternary fluids, C_2 is initially set to zero (case 1). Three other sets for surface tension coefficients are also used to study the collision dynamics between two different droplets in the partial spreading (case 2) and total spreading (cases 3 and 4) regimes. The two colliding droplets have the same densities and viscosities with $\rho_1^* = \rho_2^* = 666$ and $\eta_1^* = \eta_2^* = 119$. The other numerical parameters are $\xi = 4$, $6M_i\gamma_i/\xi = 0.02$, $\Lambda = 0.04$, and $\Psi = 0.0005$.

The droplet evolution and dimensionless kinetic energy (KE*), which is defined as $\mathrm{KE}^* = \frac{\rho u^2/2}{\rho U_{\mathrm{rel}}^2/8}$, are shown in Figs. 17

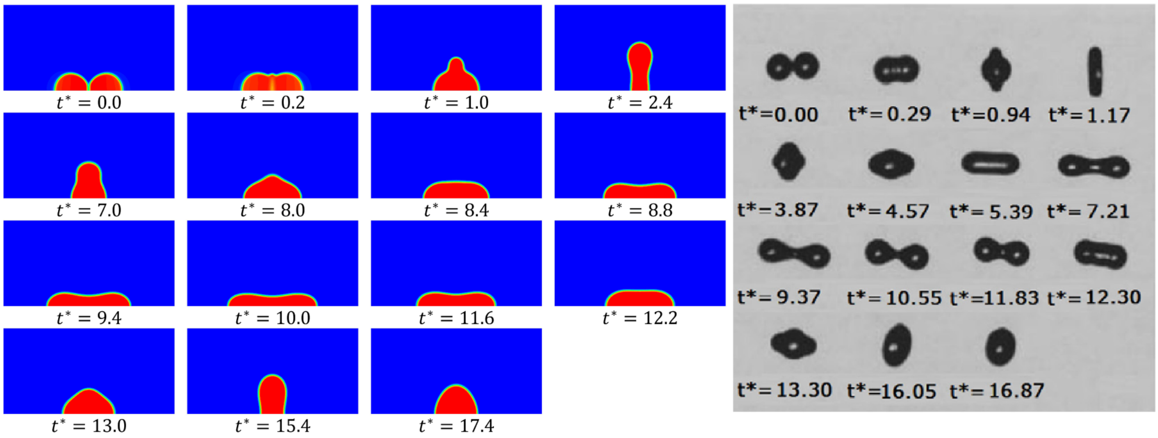

(a) (b)

FIG. 15. (a) Current results with (b) experimental work [52] ($\rho_1^* = 666$, $\eta_1^* = 119$, $\mathrm{We}_1 = 32.8$, $\mathrm{Oh}_1 = 0.615$). Note that in the current results $t^* = 0$ is adjusted to match the experimental data.

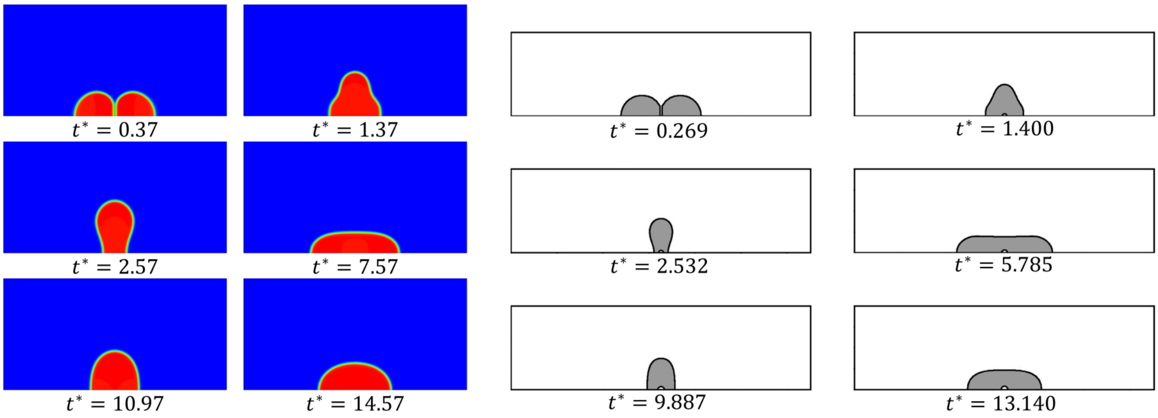

(a) (b)

FIG. 16. (a) Current results with (b) numerical work [53] ($\rho_1^* = 4$, $\eta_1^* = 4$, $\mathrm{We}_1 = 20$, $\mathrm{Oh}_1 = 0.589$).

and 18, respectively. The kinetic energy is nondimensionalized by the initial kinetic energy of the droplet. As can be seen in Fig. 17, for the binary droplet collision (the upper half of the frames in Fig. 17), the droplets coalesce at the same time ($t^* = 0.68$), similar to the ternary droplet collision (the lower half of the frames in Fig. 17). Then the two droplets get stretched vertically and become elongated at $t^* = 3.08$. In the ternary case, the outcome of the collision is a two-component droplet that breaks up at $t^* = 9.08$, whereas a relatively larger droplet is formed in the binary-fluid system. Tracking the KE* distribution reveals that the kinetic energy in the binary-fluid collision (case 1) is higher than that in the ternary-fluid system (case 2). This is due to an additional intermolecular force between two droplets of different fluid components in the ternary-fluid system.

In the total spreading regime (case 3) in Fig. 18 (the upper half of the frames), after the two droplets kiss, higher kinetic energy is released due to different surface tension coefficients. This kinetic energy is used to minimize the interface between the two components by placing another component (in this case, component 2) with a negative value of the spreading factor between them. Finally, one of the droplets is completely engulfed by the other one, forming a mixed droplet at $t^* = 6.68$.

In the other total spreading case (case 4) in Fig. 18 (the lower half of the frames), the two droplets approach each other, but the third component with a negative value of the spreading factor prevents the head-on collision. This causes the approaching droplets to stretch vertically, perpendicular to their line of motion ($t^* = 1.48$). Then, the interfacial tension forces come into play, and the two droplets recede ($t^* = 3.08$), bouncing off of each other.

In order to investigate the collision of two droplets in more detail, the total and maximum kinetic energies are plotted in Figs. 19 and 20, respectively. The total kinetic energy is defined in the dimensionless form as

$$\mathrm{KE}_{\mathrm{tot}}^* = \frac{\int_\Omega \frac{1}{2}\rho_i\left(u_x^2 + u_y^2\right)d\Omega_i}{\int_\Omega \frac{1}{8}\rho_i U_{\mathrm{rel}}^2 d\Omega_i}. \tag{29}$$

Figure 19 shows that the oscillations of the merged droplets, stemming from the head-on collision, is higher for case 1 compared with the other cases. Also, it can be seen that less than 40% of the initial total kinetic energy can be recovered after the first oscillation in both binary- and ternary-fluid collisions.

As can be seen in Fig. 20, the head-on collision in the ternary-fluid system (case 3) has the highest kinetic energy compared with the other cases. This is likely due to having higher surface tension values; the entrapment of one of the components inside the other two components could be responsible for this as well. Finally, we provide an empirical guideline as how to choose numerical parameters, such as the interface thickness ξ and mobility M_i. In general, these parameters are determined based on numerical stability and accuracy. Having a small ξ is desirable as this improves convergence towards

TABLE II. Fluid properties for different case studies.

Case study		Surface tension coefficients	Dimensionless parameters
Case 1	Binary ($C_2 = 0$)	$\sigma_{13} = 10^{-3}$	$\mathrm{We}_1 = 32.8$, $\mathrm{Oh}_1 = 0.615$
Case 2	Ternary (total spreading)	$(\sigma_{12},\sigma_{13},\sigma_{23}) = (10^{-3},10^{-3},10^{-3})$	$\mathrm{We}_1 = 32.8$, $\mathrm{Oh}_1 = 0.615$ $\mathrm{We}_2 = 32.8$, $\mathrm{Oh}_2 = 0.615$
Case 3	Ternary (total spreading)	$(\sigma_{12},\sigma_{13},\sigma_{23}) = (10^{-3},2.5 \times 10^{-3},10^{-3})$	$\mathrm{We}_1 = 13.1$, $\mathrm{Oh}_1 = 0.389$ $\mathrm{We}_2 = 32.8$, $\mathrm{Oh}_2 = 0.615$
Case 4	Ternary (total spreading)	$(\sigma_{12},\sigma_{13},\sigma_{23}) = (2.5 \times 10^{-3},10^{-3},10^{-3})$	$\mathrm{We}_1 = 32.8$, $\mathrm{Oh}_1 = 0.615$ $\mathrm{We}_2 = 32.8$, $\mathrm{Oh}_2 = 0.615$

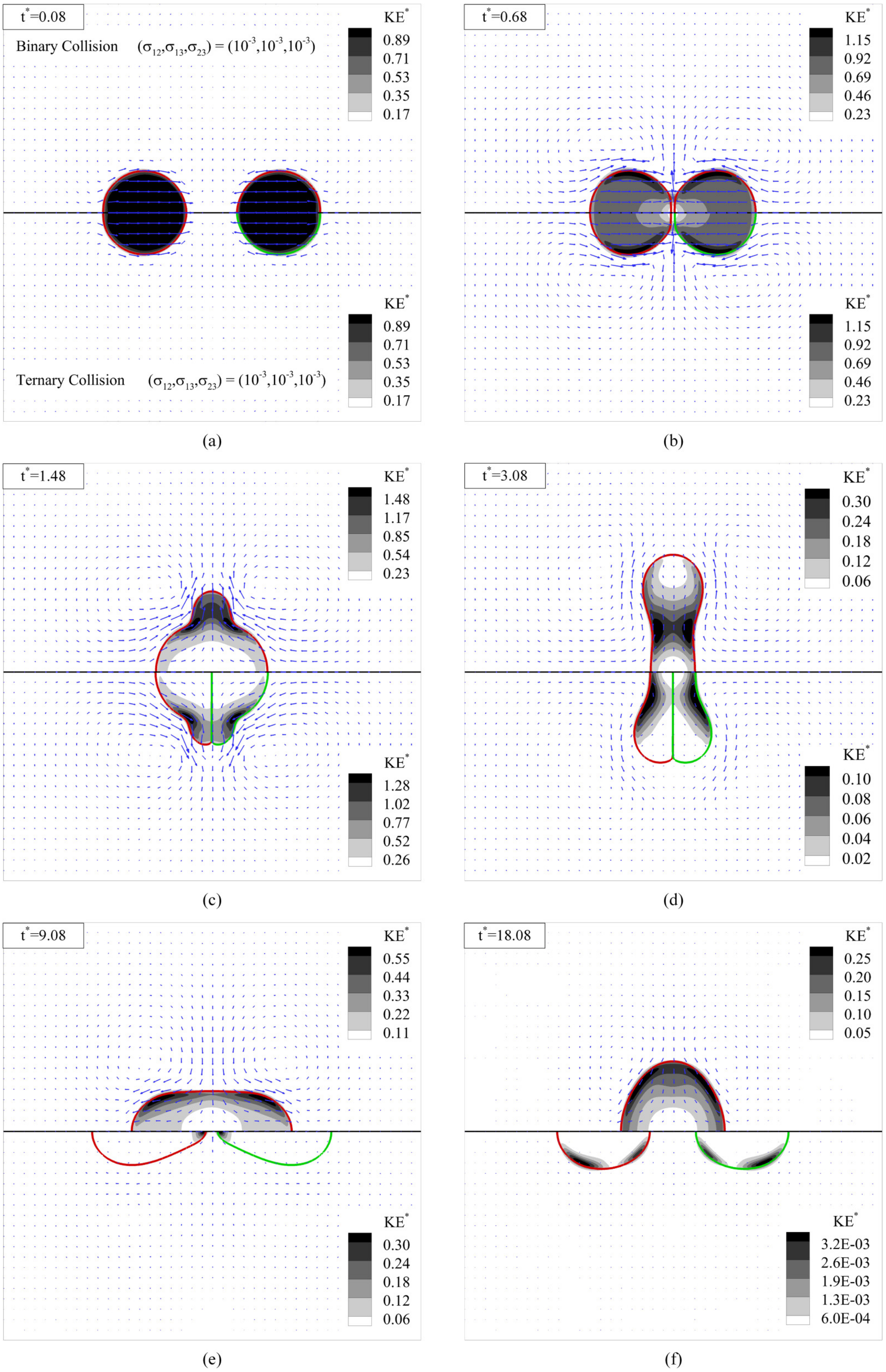

FIG. 17. Collision between two droplets. Case 1 (upper half of the frames) and case 2 (lower half of the frames). Vector lengths are the same for all results and magnified by 1000. The solid lines indicate the order parameters of $C_1 = 0.5$ (the red lines) and $C_2 = 0.5$ (the green lines).

the sharp-interface solution. A small value for ξ, however, might lead to numerical instability, especially at higher density ratios. As suggested in Ref. [54], we use $\xi = 5$ for a density ratio of 1000, whereas $\xi = 3$ is found to be sufficient when the density ratio is less than 10. Similarly, a high value for the mobility results in excessive numerical dissipation, which

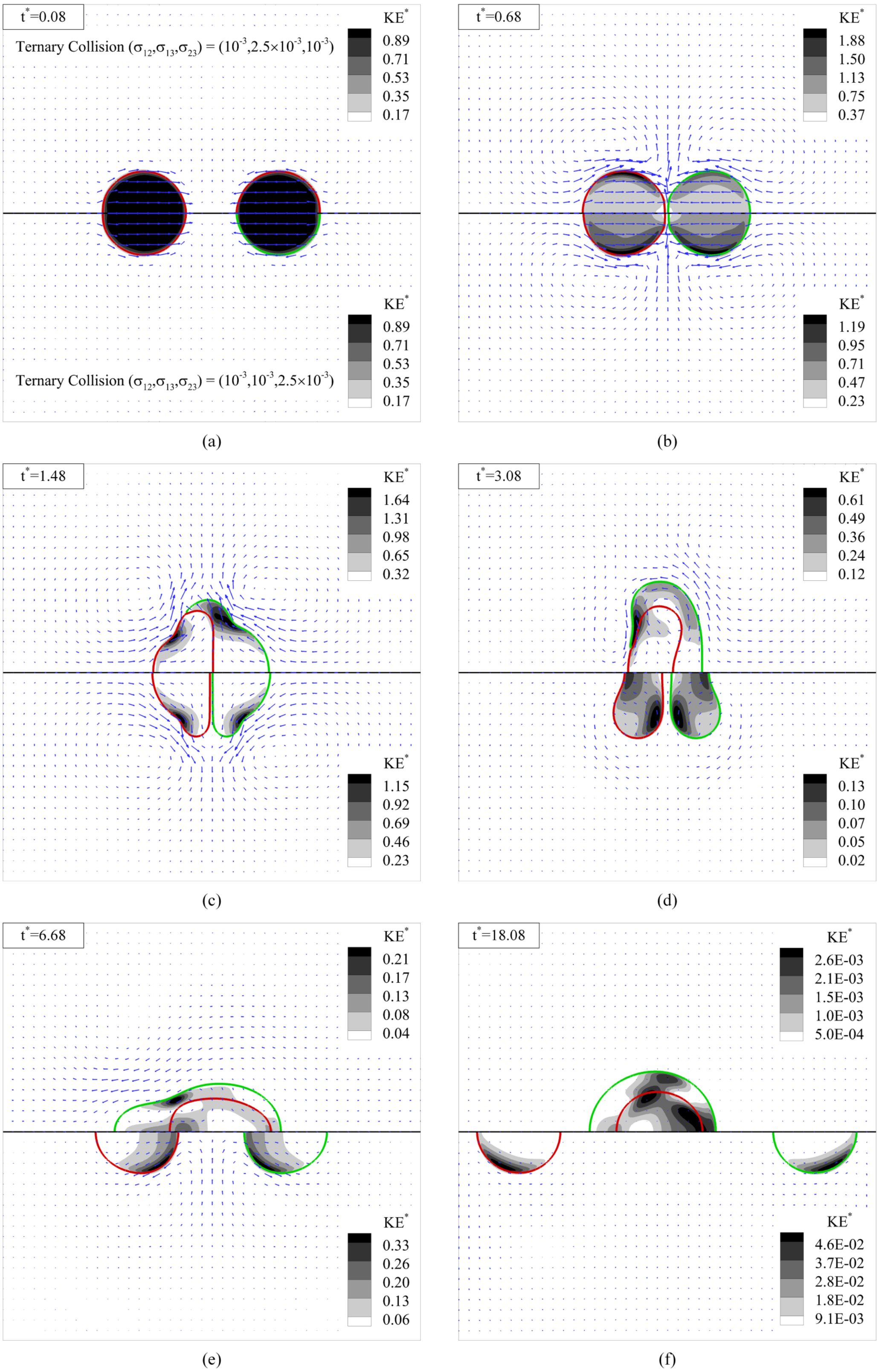

(a) (b) (c) (d) (e) (f)

FIG. 18. Collision between two droplets. Case 3 (upper half of the frames) and case 4 (lower half of the frames). Vector lengths are the same for all results and magnified by 1000. The solid lines indicate the order parameters of $C_1 = 0.5$ (the red lines) and $C_2 = 0.5$ (the green lines).

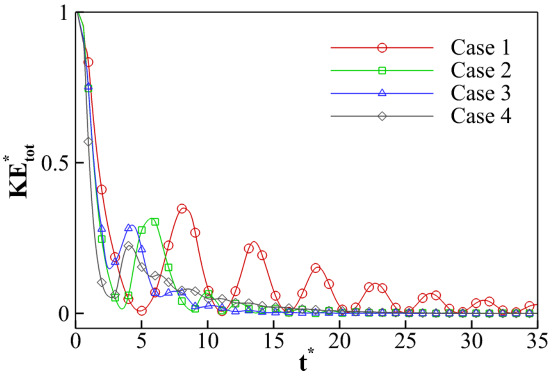

FIG. 19. Dimensionless total kinetic energy versus dimensionless time.

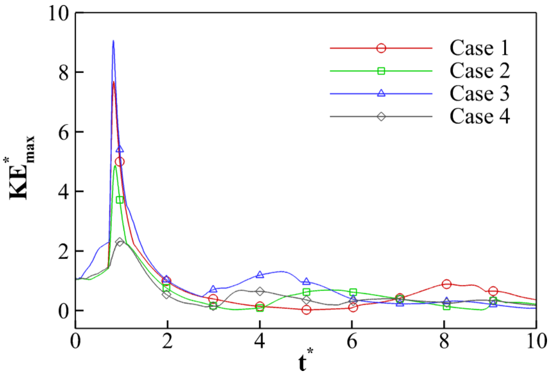

FIG. 20. Maximum dimensionless kinetic energy versus dimensionless time.

deteriorates the accuracy of the results. On the other hand, having a too small M_i might cause numerical instability. In this paper, we choose the mobility in such a way that $6M_i\gamma_i/\xi$ would be in the range of 0.014–0.03 [26] with $6M_i\gamma_i/\xi = 0.03$ for the highest density ratio and $6M_i\gamma_i/\xi = 0.014$ for low density ratios.

IV. CONCLUSIONS

A ternary LB model for simulating three-component fluid flows at high density and viscosity ratios was proposed in this paper. The proposed model is able to handle both partial and total spreadings with density and viscosity ratios of 1000 and 100, respectively, while eliminating the parasitic currents to the machine precision. Several numerical studies were carried out to test the accuracy of the model, and the results were found to be in good agreement with existing experimental and numerical data. The head-on collision between two droplets was also considered in both binary- and ternary-fluid systems. The results demonstrated the capabilities of the model in dealing with various kinds of ternary-fluid systems occurring in many natural and engineering phenomena. Although we proposed and tested the ternary LB model in 2D, its extension to 3D is straightforward and is the subject of future work.

---

[1] H.-K. Zhao, T. Chan, B. Merriman, and S. Osher, A variational level set approach to multiphase motion, J. Comput. Phys. **127**, 179 (1996).

[2] C. W. Hirt and B. D. Nichols, Volume of fluid (VOF) method for the dynamics of free boundaries, J. Comput. Phys. **39**, 201 (1981).

[3] G. Tryggvason *et al.*, A front-tracking method for the computations of multiphase flow, J. Comput. Phys. **169**, 708 (2001).

[4] X. He and L.-S. Luo, Theory of the lattice Boltzmann method: From the Boltzmann equation to the lattice Boltzmann equation, Phys. Rev. E **56**, 6811 (1997).

[5] X. He and G. D. Doolen, Thermodynamic foundations of kinetic theory and lattice Boltzmann models for multiphase flows, J. Stat. Phys. **107**, 309 (2002).

[6] S. Williams, J. Carter, L. Oliker, J. Shalf, and K. Yelick, Optimization of a lattice Boltzmann computation on state-of-the-art multicore platforms, J. Parallel Distrib. Comput. **69**, 762 (2009).

[7] M. Schönherr, K. Kucher, M. Geier, M. Stiebler, S. Freudiger, and M. Krafczyk, Multi-thread implementations of the lattice Boltzmann method on non-uniform grids for CPUs and GPUs, Comput. Math. Appl. **61**, 3730 (2011).

[8] K. Connington and T. Lee, Lattice Boltzmann simulations of forced wetting transitions of drops on superhydrophobic surfaces, J. Comput. Phys. **250**, 601 (2013).

[9] A. K. Gunstensen, D. H. Rothman, S. Zaleski, and G. Zanetti, Lattice Boltzmann model of immiscible fluids, Phys. Rev. A **43**, 4320 (1991).

[10] X. Shan and H. Chen, Lattice Boltzmann model for simulating flows with multiple phases and components, Phys. Rev. E **47**, 1815 (1993).

[11] M. R. Swift, E. Orlandini, W. R. Osborn, and J. M. Yeomans, Lattice Boltzmann simulations of liquid-gas and binary fluid systems, Phys. Rev. E **54**, 5041 (1996).

[12] X. He, S. Chen, and R. Zhang, A lattice Boltzmann scheme for incompressible multiphase flow and its application in simulation of Rayleigh–Taylor instability, J. Comput. Phys. **152**, 642 (1999).

[13] A. Mazloomi M, S. S. Chikatamarla, and I. V. Karlin, Entropic Lattice Boltzmann Method for Multiphase Flows, Phys. Rev. Lett. **114**, 174502 (2015).

[14] D. Lycett-Brown, K. H. Luo, R. Liu, and P. Lv, Binary droplet collision simulations by a multiphase cascaded lattice Boltzmann method, Phys. Fluids **26**, 023303 (2014).

[15] Q. Li, K. H. Luo, Q. J. Kang, Y. L. He, Q. Chen, and Q. Liu, Lattice Boltzmann methods for multiphase flow and phase-change heat transfer, Prog. Energy Combust. Sci. **52**, 62 (2016).

[16] H. Liu *et al.*, Multiphase lattice Boltzmann simulations for porous media applications, Comput. Geosci. **20**, 777 (2016).

[17] S. Leclaire, M. Reggio, and J.-Y. Trépanier, Progress and investigation on lattice Boltzmann modeling of multiple immiscible fluids or components with variable density and viscosity ratios, J. Comput. Phys. **246**, 318 (2013).

[18] T. Reis and T. Phillips, Lattice Boltzmann model for simulating immiscible two-phase flows, J. Phys. A: Math. Theor. **40**, 4033 (2007).

[19] J. Bao and L. Schaefer, Lattice Boltzmann equation model for multi-component multi-phase flow with high density ratios, Applied Mathematical Modelling **37**, 1860 (2013).

[20] C. Semprebon, T. Krüger, and H. Kusumaatmaja, Ternary free-energy lattice Boltzmann model with tunable surface tensions and contact angles, Phys. Rev. E **93**, 033305 (2016).

[21] Y. Shi, G. H. Tang, and Y. Wang, Simulation of three-component fluid flows using the multiphase lattice Boltzmann flux solver, J. Comput. Phys. **314**, 228 (2016).

[22] H. Liang, B. C. Shi, and Z. H. Chai, Lattice Boltzmann modeling of three-phase incompressible flows, Phys. Rev. E **93**, 013308 (2016).

[23] A. Lamura, G. Gonnella, and J. M. Yeomans, A lattice Boltzmann model of ternary fluid mixtures, Europhys. Lett. **45**, 314 (1999).

[24] H. Chen, B. M. Boghosian, P. V. Coveney, and M. Nekovee, A Ternary Lattice Boltzmann Model for Amphiphilic Fluids, Proc. R. Soc. London, Ser. A **456**, 2043 (2000).

[25] M. Nekovee, P. V. Coveney, H. Chen, and B. M. Boghosian, Lattice-Boltzmann model for interacting amphiphilic fluids, Phys. Rev. E **62**, 8282 (2000).

[26] T. Lee and L. Liu, Lattice Boltzmann simulations of micron-scale drop impact on dry surfaces, J. Comput. Phys. **229**, 8045 (2010).

[27] T. Lee, Effects of incompressibility on the elimination of parasitic currents in the lattice Boltzmann equation method for binary fluids, Comput. Math. Appl. **58**, 987 (2009).

[28] A. Fakhari and T. Lee, Multiple-relaxation-time lattice Boltzmann method for immiscible fluids at high Reynolds numbers, Phys. Rev. E **87**, 023304 (2013).

[29] H. Safari, M. H. Rahimian, and M. Krafczyk, Extended lattice Boltzmann method for numerical simulation of thermal phase change in two-phase fluid flow, Phys. Rev. E **88**, 013304 (2013).

[30] H. Safari, M. H. Rahimian, and M. Krafczyk, Consistent simulation of droplet evaporation based on the phase-field multiphase lattice Boltzmann method, Phys. Rev. E **90**, 033305 (2014).

[31] A. Begmohammadi, M. Farhadzadeh, and M. H. Rahimian, Simulation of pool boiling and periodic bubble release at high density ratio using lattice Boltzmann method, Int. Commun. Heat Mass Transfer **61**, 78 (2015).

[32] A. Begmohammadi, M. Rahimian, M. Farhadzadeh, and M. A. Hatani, Numerical simulation of single-and multi-mode film boiling using lattice Boltzmann method, Comput. Math. Appl. **71**, 1861 (2016).

[33] M. Ashna and M. H. Rahimian, LMB simulation of head-on collision of evaporating and burning droplets in coalescence regime, Int. J. Heat Mass Transfer **109**, 520 (2017).

[34] M. Ashna, M. H. Rahimian, and A. Fakhari, Extended lattice Boltzmann scheme for droplet combustion, Phys. Rev. E **95**, 053301 (2017).

[35] D. Jacqmin, An energy approach to the continuum surface tension method, in *34th Aerospace Sciences Meeting and Exhibit, Aerospace Sciences Meetings, Reno, NV, 1996* (American Institute of Aeronautics and Astronautics, Reston, VA, 1996).

[36] F. Boyer and C. Lapuerta, Study of a three component Cahn-Hilliard flow model, ESAIM: Math. Modell. Numer. Anal. **40**, 653 (2006).

[37] F. Boyer, C. Lapuerta, S. Minjeaud, B. Piar, and M. Quintard, Cahn–Hilliard/Navier–Stokes model for the simulation of three-phase flows, Transp. Porous Media **82**, 463 (2010).

[38] T. Inamuro, S. Tajima, and F. Ogino, Lattice Boltzmann simulation of droplet collision dynamics, Int. J. Heat Mass Transf. **47**, 4649 (2004).

[39] Y. Y. Yan and Y. Q. Zu, A lattice Boltzmann method for incompressible two-phase flows on partial wetting surface with large density ratio, J. Comput. Phys. **227**, 763 (2007).

[40] J. Gong, N. Oshima, and Y. Tabe, Spurious velocity from the cutoff and magnification equation in free energy-based LBM for two-phase flow with a large density ratio, Comput. Math. Appl. (2016).

[41] X. He, X. Shan, and G. D. Doolen, Discrete Boltzmann equation model for nonideal gases, Phys. Rev. E **57**, R13(R) (1998).

[42] J. Kim, Phase field computations for ternary fluid flows, Comput. Methods Appl. Mech. Eng. **196**, 4779 (2007).

[43] R.-H. Chen, Diesel–diesel and diesel–ethanol drop collisions, Appl. Therm. Eng. **27**, 604 (2007).

[44] R.-H. Chen and C.-T. Chen, Collision between immiscible drops with large surface tension difference: diesel oil and water, Exp. Fluids **41**, 453 (2006).

[45] T.-C. Gao, R.-H. Chen, J.-Y. Pu, and T.-H. Lin, Collision between an ethanol drop and a water drop, Exp. Fluids **38**, 731 (2005).

[46] C. Planchette, E. Lorenceau, and G. Brenn, Liquid encapsulation by binary collisions of immiscible liquid drops, Colloids Surf., A **365**, 89 (2010).

[47] I. V. Roisman, C. Planchette, E. Lorenceau, and G. Brenn, Binary collisions of drops of immiscible liquids, J. Fluid Mech. **690**, 512 (2012).

[48] G. Li *et al.*, Incompressible multiphase flow and encapsulation simulations using the moment-of-fluid method, Int. J. Numer. Methods Fluids **79**, 456 (2015).

[49] M. Wöhrwag, C. Semprebon, A. M. Moqaddam, I. Karlin, and H. Kusumaatmaja, Ternary free-energy entropic lattice Boltzmann model with high density ratio, arXiv:1710.07486.

[50] C. Planchette, E. Lorenceau, and G. Brenn, The onset of fragmentation in binary liquid drop collisions, J. Fluid Mech. **702**, 5 (2012).

[51] D. Quéré, Water colliding with oil, J. Fluid Mech. **702**, 1 (2012).

[52] J. Qian and C. K. Law, Regimes of coalescence and separation in droplet collision, J. Fluid Mech. **331**, 59 (1997).

[53] K. N. Premnath and J. Abraham, Simulations of binary drop collisions with a multiple-relaxation-time lattice-Boltzmann model, Phys. Fluids **17**, 122105 (2005).

[54] A. Fakhari, D. Bolster, and L.-S. Luo, A weighted multiple-relaxation-time lattice Boltzmann method for multiphase flows and its application to partial coalescence cascades, J. Comput. Phys. **341**, 22 (2017).